Manuscript

1
2
3
4
5
6
7
8
9
10
11
12
13
14
15
16
17
18
19
20
21
22
23
24
25
26
27
28
29
30
31
32
33
34
35
36
37
38
39
40
41
42
43
44
45
46
47
48
49
50
51
52
53
54
55
56
57
58
59
60
61
62
63
64
65

Simulation of the spin–polarization and the charge transport in Zener tunnel junctions based on ferromagnetic GaAs and ZnO

E. Comesaña[a,*], M. Aldegunde[b], A.J. Garcia–Loureiro[a]

[a] *Departamento de Electrónica e Computación, Universidade de Santiago de Compostela, 15782 Santiago de Compostela (Spain)*
[b] *College of Engineering, Swansea University, SA2 8PP Swansea (United Kingdom)*

Abstract

Simulation of the tunneling current as a function of voltage for a Zener diode where both sides are ferromagnetic have been performed. The current is evaluated as a function of the voltage and of the magnetization on each side of the diode. Calculations are made using an in–house developed simulator which solves Poisson, electron and hole continuity equation self–consistently. The drift–diffusion model is used to calculate the charge carrier distribution. The current expressions were modified to consider degenerate semiconductors. Our simulator includes a non–local tunneling transport model which was modified to account for the spin polarization of the carriers. The tunneling magnetoresistance is obtained from the I–V characteristics for parallel and antiparallel configurations of the magnetization vectors in each side of the device. Two different devices were analyzed, one that corresponds to Mn doped GaAs in which the ferromagnetism is stronger on the p side of the diode and the other that corresponds to ZnO where there are likely to be many more carriers on the n side of the diode. We found good agreement between the results of our simulations and the theoretical predictions of the tunneling magnetoresistance, especially at room temperature. We also found that larger band–gap materials show larger tunneling current but lower tunnel magnetoresistance.

Keywords: Magnetoelectronics, spintronics, spin polarized transport in semiconductors, junction diodes, tunneling, III–V semiconductors, II–VI semiconductors, GaAs, ZnO

1. Introduction

Diluted magnetic semiconductor (DMS) are considered to be a new generation materials with the most potential for the future developing of new spintronic technologies and new spin based device applications. DMSs provide simultaneous control on the flow of the carrier charge and spin[1]. Spintronics is motivated by the belief that spin signal processing may yield advantages in terms of processing speed, power consumption or device density.

Since the prediction of high Curie temperature DMSs, based on III–V semiconductors [2], the search of such materials is receiving much attention as they are keystone for the developing of spintronics. In an optimally doped DMS the density of carriers is approximately half of the density of magnetic ions which is usually between $x = 5\%$ and $x = 15\%$ (x is the fraction of magnetic ions added to the semiconductor). The well established DMS occur with one type of carrier. One of the most investigated materials is the III–V material $(Ga_{1-x}Mn_x)As$ in which the Mn ion provides a localized spin $S = 5/2$ and also contributes a hole [3]. The holes are degenerate and strongly polarized at low temperatures [4]. Despite the fact that non-ferromagnetic GaAs is easy to dope to both p type and n type, the ferromagnetic III–V doped materials are all p type. However there is much effort to find a compatible n type ferromagnetic semiconductor [5, 6]. Magnetic properties have been seen also in a number of magnetically doped oxides, particularly ZnO, TiO_2 and SnO_2 [7–9] all of which occur as n type semiconductors. Even though there are experimental evidence of p-type ZnO, it is extremely difficult to dope and the samples show very low conductivity and still they are not in the Zener regime [10, 11]. There is growing interest in the developing of magnetic tunnel junctions based on $(Zn_{1-x}Co_x)O$ with different barriers [12, 13] because of its high Curie temperature and promising magnetotransport [14–16].

A pn junction of two highly degenerated semiconductors makes a tunneling diode which has many applications [17] and adding magnetic functionality would enable more devices such as magnetic switching of microwave devices. Zener tunneling has been observed in a ferromagnetic/nonmagnetic (GaMn)As/GaAs heterostructure [18] and a high spin polarization is observed optically [19]. The voltage dependence of the tunneling current in a spin–polarized Zener diode, as shown in figure 1, is well fitted by the theory of a non–magnetic diode [4]. We are developing analytical [20] and numerical models [21] to study the transport in ferromagnetic Zener diodes. Using these models we have predicted the dependence of the tunneling current on the mean magnetization of the system and we

*Corresponding author
Email address: enrique.comesana@usc.es (E. Comesaña)

have evaluated the tunneling magnetoresistance (TMR) in a theoretical both–sided–ferromagnetic diode with different spin–polarization ratios.

The charge and spin transport is simulated using the drift–diffusion model [22, 23]. Our simulator solves the Poisson and the electron and hole continuity equations self–consistently using the finite difference technique. The tunneling current is added to the total current using a generation–recombination term. This term has been modified to take into account the different spin of the carriers and therefore which of the tunneling assisted generation–recombination processes are allowed depending on the spin of the involved carriers.

The present paper is structured as follows: In section 2 we show the structure of our in–house simulator; section 3 explains the origin of the tunneling current and how it is modeled in our simulator; section 4 shows the simulation results performed on GaAs and ZnO diodes using two commercial simulators, Atlas [24] from Silvaco and Sentaurus Device [25] from Synopsys, and our simulator; in section 5 we explain how we model the spin splitting in our simulator; in sections 6 and 7 we show the obtained results for the simulations of the GaAs and ZnO based diodes also comparing the results; finally the conclusions of this work are summarized in section 8.

2. Simulator structure

Figure 2 shows the main steps of our in–house simulator which mainly accounts the tunneling current through the device as it is the main contribution to the TMR in Zener diodes. Our simulator solves the Poisson equation coupled with the electron and hole continuity equations. It adds a tunneling generation/recombination term to the continuity equations which is explained in next section. This term is very sensitive to the shape of the energy band edges in two ways: the band edges determine the tunneling probability as the potential barrier changes with them and also to the local electric field that is affecting to the carrier that is suffering the tunneling process. Therefore, the model to obtain the spin–split energy bands will be a sensitive factor in the final obtained TMR.

Our simulator has been developed to deal with degenerate semiconductor based devices. Both GaAs and ZnO doped with Mn or Co show high carrier concentration with the Fermi energy level in the carrier energy band instead of the band gap. Therefore we have to implement modifications on the drift–diffusion model of the current through the device to consider degeneration, thus avoiding the exponential approximation of the Fermi function in the carrier density calculation [26].

The expressions for the electron and hole currents are obtained from the Boltzman transport equation (BTE) using a number of simplifications:

$$\vec{J_n} = -q_e \mu_n n \nabla \phi_n \tag{1}$$

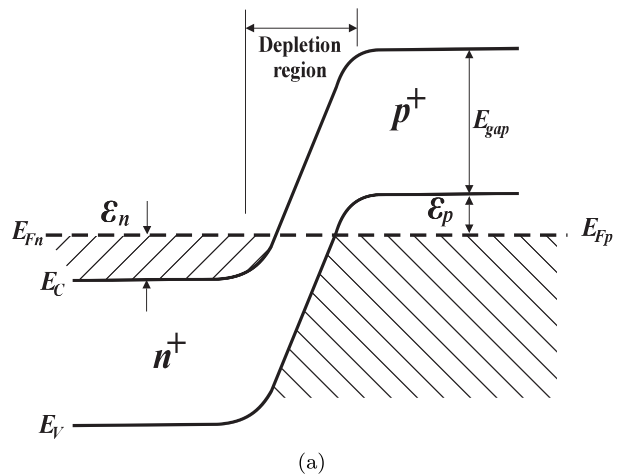

(a)

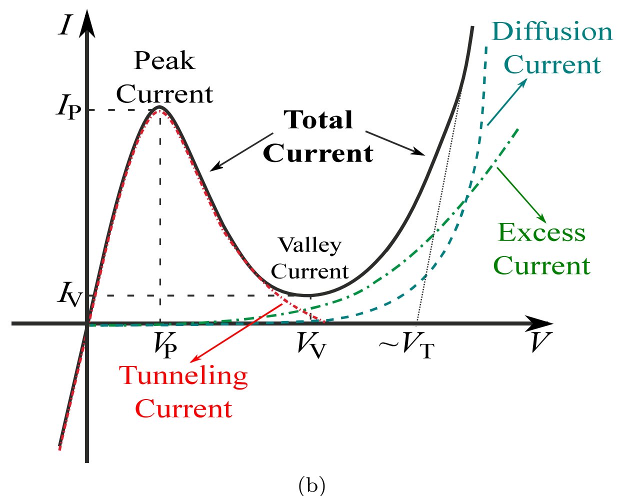

(b)

Figure 1: (a) Tunnel diode band diagram and (b) typical I–V characteristic, showing the three contributions to the total current: tunnel, excess and diffusion currents.

$$\vec{J_p} = -q_e \mu_p p \nabla \phi_p, \tag{2}$$

where ϕ_n, ϕ_p are the Fermi pseudo–potentials and μ_n, μ_p are the mobilities for electrons and holes respectively.

The equations for the carrier currents can be expressed in terms of a a drift term plus a diffusion term using the carrier concentration formula, i.e. for electrons, assuming parabolic bands:

$$n = N_c F_{1/2}(\eta_n), \tag{3}$$

where

$$\eta_n = \frac{E_{Fn} - E_C}{K_B T} \tag{4}$$

and $F_{1/2}(\eta_n)$ is the complete Fermi integral of index 1/2 for the electrons in the conduction band.

The carrier concentration gradient can be expressed as

$$\begin{aligned} \nabla n &= N_c \nabla F_{1/2}(\eta_n) = N_c F_{-1/2}(\eta_n) \nabla \eta_n = \\ &= N_c F_{-1/2}(\eta_n) \frac{\nabla E_{Fn} - \nabla E_C}{K_B T}, \end{aligned} \tag{5}$$

where the derivative of the complete Fermi–Dirac integral of index 1/2, $F_{1/2}(\eta_n)$, is calculated using the following

property of the complete Fermi–Dirac integral of index ν, $F_\nu(\eta)$, is

$$\frac{d}{d\eta}F_\nu\left(\eta\right)=F_{\nu-1}\left(\eta\right), \tag{6}$$

and

$$F_\nu=\frac{1}{\Gamma(\nu+1)}\int_0^\infty\frac{t^\nu}{\exp(t-x)+1}dt \tag{7}$$

where $\Gamma(\nu+1)$ is the gamma function.

Using that $E_{Fn}=-q_e\phi_n$,

$$-q_e\nabla\phi_n=\frac{K_BT}{N_cF_{-1/2}\left(\eta_n\right)}\nabla n+\nabla E_C, \tag{8}$$

therefore the electron current expression (1) can be reformulated as

$$\begin{aligned}\vec{J}_n &= \mu_n n\left(\frac{K_BT}{N_cF_{-1/2}\left(\eta_n\right)}\nabla n+\nabla E_C\right)\\ &= \mu_n\left(\frac{F_{1/2}\left(\eta_n\right)}{F_{-1/2}\left(\eta_n\right)}K_BT\nabla n+n\nabla E_C\right),\end{aligned} \tag{9}$$

and using a similar procedure we can obtain the hole current expression

$$\vec{J}_p=-\mu_p\left(\frac{F_{1/2}\left(\eta_p\right)}{F_{-1/2}\left(\eta_p\right)}K_BT\nabla p-p\nabla E_V\right). \tag{10}$$

In previous equations, ∇E_C and ∇E_V is the local electric field in the device and the factors $\frac{F_{1/2}(\eta_n)}{F_{-1/2}(\eta_n)}$, $\frac{F_{1/2}(\eta_p)}{F_{-1/2}(\eta_p)}$ can be interpreted as correction factors to the diffusion coefficients to account for the local degeneration level of the semiconductor.

The equations for the drift–diffusion model, obtained from the BTE, are quite limited due to the considered simplifications. They are only valid when the electric field takes relatively low values. Moreover, although we have included a degeneration factor to consider high carrier concentrations, this approximation is very limited because parabolic bands are considered in the BTE simplification and this becomes false as the degeneration increases. However, bearing in mind that we are in the limit of the domain of validity of the drift–diffusion model, we still have performed the simulations using this model because of the computational low–cost of the calculations and also because it still can give some important insight into the behavior of such ferromagnetic devices.

The simulator initially solves the Poisson equation using Neuman boundary conditions to obtain a first solution to the electrostatic potential and carrier concentrations. After this, it performs two external iterations to solve the Poisson equation and the electron and hole continuity equations self–consistently, using Dirichlet boundary conditions: in the first iteration it solves those three equations without considering tunneling to obtain a first approach to the solution under a certain bias. In the second iteration, it will add the tunneling current as a recombination term to the continuity equations to obtain the final solution. This

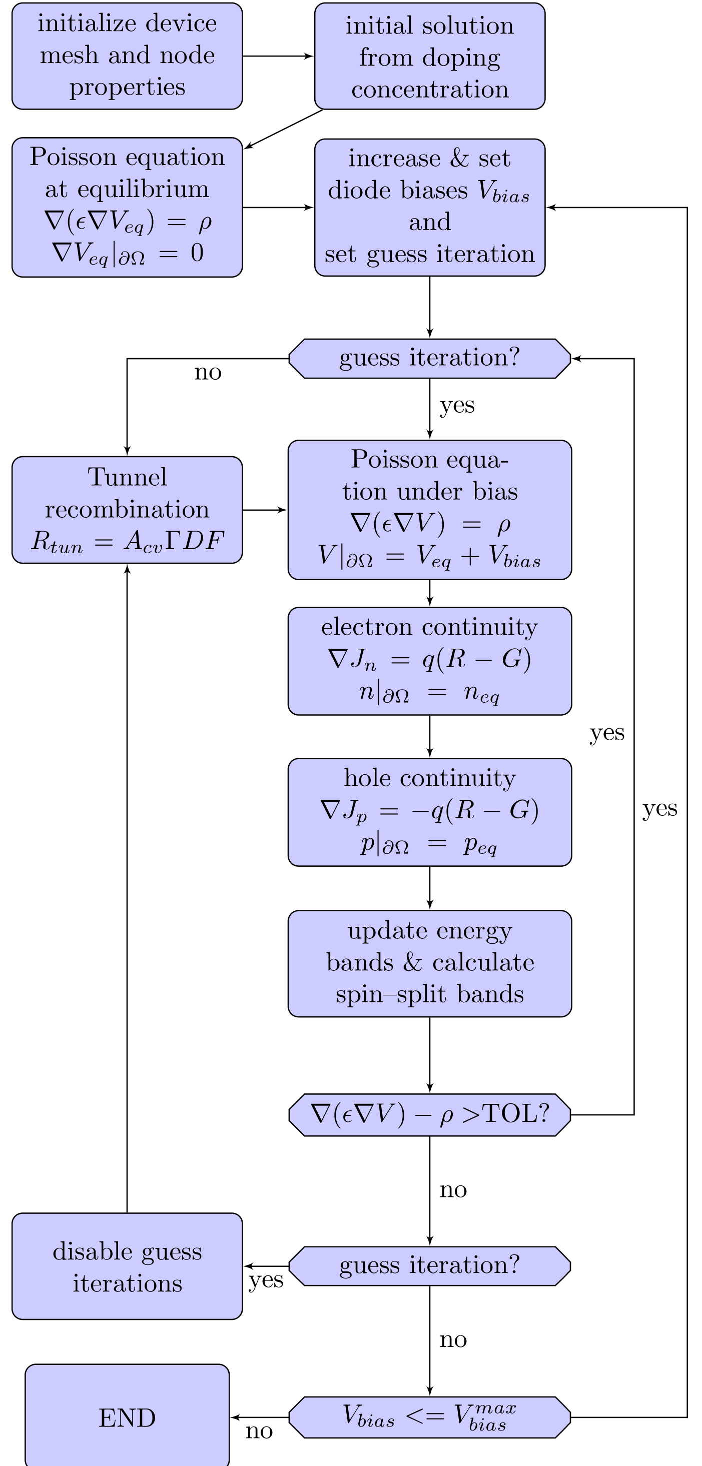

Figure 2: General flow chart of our in–house simulator.

solution in two steps adds stability to the convergence of the resolution of the system of three differential equations.

A general iteration of the simulator consists of the solution of these three equations:

$$\left\{ \begin{array}{ccc} \nabla(\epsilon\nabla V) & = & q_e\left(p-n+N_D^+-N_A^-\right) \\ \nabla\vec{J_n} & = & q_e\left(R_{tun}^{e^\uparrow-h^\downarrow}+R_{tun}^{e^\downarrow-h^\uparrow}\right) \\ \nabla\vec{J_p} & = & -q_e\left(R_{tun}^{e^\uparrow-h^\downarrow}+R_{tun}^{e^\downarrow-h^\uparrow}\right) \end{array} \right\} \quad (11)$$

where ϵ is the dielectric constant, V the electrostatic potential, N_D^+ the concentration of ionized donor impurities, N_A^- the concentration of ionized acceptor impurities, $R_{tun}^{e^\uparrow-h^\downarrow}$ the tunneling recombination term of spin–up electrons with spin–down holes and $R_{tun}^{e^\downarrow-h^\uparrow}$ the tunneling recombination term of spin–down electrons with spin–up holes. The model used in the calculation of these two terms is explained in next section. Finally, after solving those tree equations, the energy bands are updated and the spin–splitting energy is recalculated using the model explained in section 5.

3. Tunneling recombination term

The current through a tunneling diode has three components [17]: the tunneling current, the excess current and the diffusion current. The tunneling current is expected to rise to a maximum at low voltage, about the smallest of the distances between the Fermi level and the conduction band in the n–side (ε_n/q_e) and the valence band in the p–side (ε_p/q_e), we call ε_S/q_e to the smallest distance opposed to ε_L/q_e the largest distance. Then it falls to zero when the bias increases over $(\varepsilon_n+\varepsilon_p)/q_e$ or $(\varepsilon_S+\varepsilon_L)/q_e$, see figure 1. This fall in the I–V curve is known as negative resistance region (NRR) and is produced by the reduction of the overlapping of the density of carrier functions in both p and n sides [27] and the decrease of the tunneling probability as the bias is increased. The last two components of the current, the excess and diffusion currents, become important for higher voltages out of the range of interest in this paper.

The tunneling of carriers through the band–gap is an important part of the carrier transport in highly doped pn junctions. There are two tunneling mechanisms: the direct transition from band to band and the trap assisted tunneling. The basic principles of the band–to–band tunneling were explained by Kane [27]. The tunneling probability at a energy level (ε), obtained from the Wentzel–Kramers–Brioullin (WKB) two–band approximation, is given by

$$\Gamma(\varepsilon) \simeq \exp\left[-2\int_l^u |\kappa(\mathbf{r})|d\mathbf{r}\right], \quad (12)$$

where $\kappa(\mathbf{r})$ is the evanescent wave vector associated to the carrier near the barrier and u and l are the classical turning points in the potential barrier, defined by the band edges as shown in figure 3, where

$$\kappa(\mathbf{r}) = \frac{\kappa_e\kappa_h}{\sqrt{\kappa_e^2+\kappa_h^2}} \quad (13)$$

and

$$\kappa_e = \frac{1}{i\hbar}\sqrt{2m_0m_e(\varepsilon-E_C)} \quad (14)$$

$$\kappa_h = \frac{1}{i\hbar}\sqrt{2m_0m_h(E_V-\varepsilon)} \quad (15)$$

with E_C and E_V the conduction and valence band edge energy in the classical turning points, respectively. The combination of the two electron and hole wave vector ensures that the tunneling is electron like near the conduction band, hole like near the valence band and mixed around mid–bandgap energies.

The tunneling current density is described as follows:

$$J_{tun}(\varepsilon) = \frac{q}{\pi\hbar}\int \Gamma(\varepsilon)\rho_t[f_u(\varepsilon+\varepsilon_t)-f_l(\varepsilon+\varepsilon_t)]d\varepsilon d\varepsilon_t \quad (16)$$

where $\rho_t = \frac{\sqrt{m_e^*m_h^*}}{2\pi\hbar^2}$ is the 2–dimensional density of states related to the two transversal wave–vectors, and f_l and f_u are the Fermi–Dirac functions evaluated using the pseudo–Fermi level for the majority carrier at the position of classical turning points [27].

The integral over the transversal energy ε_t can be solved considering that the total energy of the carrier must be in the range $\varepsilon_{lower} \leq \varepsilon+\varepsilon_t \leq \varepsilon_{upper}$, see figure 3. The tunneling current for an energy range $\Delta\varepsilon$ is

$$\Delta J_{tun}(\varepsilon) = \frac{qk_BT\sqrt{m_e^*m_h^*}}{2\pi^2\hbar^3}\times\Gamma(\varepsilon)\times D(\varepsilon)\times\Delta\varepsilon, \quad (17)$$

where $D(\varepsilon)$ evaluates the energy overlapping of the carriers at each side of the junction, measuring the number of carriers available to tunnel with energy ε through the depletion region from a classical turning point l to u or vice versa. It can be expressed as

$$D(\varepsilon) = \log\left\{\frac{\left[1+\exp\left(\frac{E_{Fl}-\varepsilon}{k_BT}\right)\right]}{\left[1+\exp\left(\frac{E_{Fu}-\varepsilon}{k_BT}\right)\right]}\times \frac{\left[1+\exp\left(\frac{E_{Fu}-\varepsilon-\varepsilon_{\max}}{k_BT}\right)\right]}{\left[1+\exp\left(\frac{E_{Fl}-\varepsilon-\varepsilon_{\max}}{k_BT}\right)\right]}\right\}. \quad (18)$$

In this expression $\varepsilon_{\max} = \min(\varepsilon-\varepsilon_{lower}, \varepsilon_{upper}-\varepsilon)$ is the maximum transversal energy, ε_t, corresponding to a specific value of the energy "component" in the transport direction, ε, and E_{Fl} and E_{Fu} are the values of the pseudo–Fermi levels of the majority carrier at the turning point l and u respectively.

The tunneling current can be added to the electron and hole continuity equations as a non–local generation–recombination term (R_{tun}) using that

$$R_{tun}^u = \frac{1}{q}\nabla J_{tun} = \frac{1}{q}\frac{dJ_{tun}}{d\psi}\nabla\psi = \left[\frac{dJ_{tun}}{d\varepsilon}\times F\right]_u \quad (19)$$

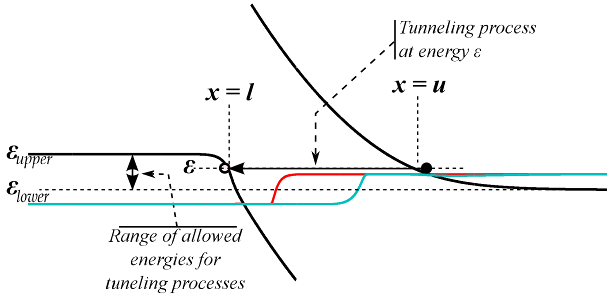

Figure 3: Schematic representation of a tunneling process at energy ε. The figure shows the classical turning points ($x = u$ and $x = l$), the range of allowed energies and the electron and hole pseudo–Fermi levels (red and blue lines, respectively) which inform about the filling of the conduction and valence band, respectively.

where ψ is the electrostatic potential , $F = -\nabla\psi$ is the electric field, and $E_C = -q\psi$ is equal to the energy of the carrier in the turning point, i.e., $\varepsilon = E_C(x = u)$. And using a similar analysis in the other turning point, the tunnel recombination term in the turning points for a given energy is

$$R^{l,u}_{tun} = \frac{qk_BT\sqrt{m^*_e m^*_h}}{2\pi^2\hbar^3} \times \Gamma^{l,u} \times F^{l,u} \times D^{l,u}. \quad (20)$$

3.1. Tunneling in Atlas

One of the two tools compared with our in–house developed simulator is Atlas [24] from Silvaco. This simulator solves the Poisson's equation, the continuity equations, the transport equations using the drift–diffusion and the energy balance transport models.

The non-local tunneling current model is implemented following the same equations as explained before. The main difference from our simulator is that Atlas calculates tunneling current using equation (17) and then injects the obtained current in the classical turning points $x = u$ and $x = l$. However we calculate the recombination term in equation (20) and then we add it to the continuity equations. We found that this approach is more stable for the convergence of the solution of the continuity equations, allowing larger degenerations and therefore larger carrier concentrations in the semiconductors.

3.2. Tunneling in Sentaurus Device

The other tool compared with our simulator is Sentaurus Device [25] from Synopsys. This simulator also solves the Poisson's equation, the continuity equations and the transport equations obtained form the drift–diffusion model, the thermodynamic model [28] or the hydrodynamic model. It also can solve temperature equations for the lattice and carriers.

The non–local tunneling current model also evaluates the total current that flows to the conduction band in point $x = u$ from the valence band at position $l < u$. Sentaurus Device calculates a recombination rate for the valence–band electrons with energy ε at a point $x = l$ (or, the generation rate of holes at $x = l$) due to the tunneling processes to or from the conduction band at $x = u$ as

$$\begin{aligned} &G_{CV}(u,l,\varepsilon) - R_{CV}(u,l,\varepsilon) = \\ &= \frac{qA_{CV}}{2qk_B}\vartheta\left[\varepsilon - E_V(l)\left.\frac{dE_V}{dl}\right|_l\right]\vartheta\left[\varepsilon - E_C(u)\left.\frac{dE_C}{du}\right|_u\right]\times \\ &\times \Gamma_{CV}(u,l,\varepsilon) \times [T_p(l) - T_n(u)] \times \\ &\times \left\{\left[1 + \exp\left(\frac{\varepsilon - E_{F,u}}{k_BT_n(u)}\right)\right]^{-1} - \right. \\ &\left. - \left[1 + \exp\left(\frac{\varepsilon - E_{F,l}}{k_BT_p(l)}\right)\right]^{-1}\right\}, \end{aligned} \quad (21)$$

where A_{CV} is a fitting parameter (also called the effective Richardson constant), T_p and T_n are the carrier temperatures, $\vartheta(x,y) = \delta(x)|y|\Theta(y)$ and Γ_{CV} is the tunneling probability obtained from the WKB approximation (see equation (12)). The current density of electrons that tunnel form the valence band at all point above $x = u$ to the conduction band at a point $x = u$ is obtained integrating over the recombination rate (equation (21)):

$$J_{CV}(u) = \iint_{u\,-\infty}^{\infty\,\infty} [G_{CV}(u,r,\varepsilon) - R_{CV}(u,r,\varepsilon)]\,d\varepsilon dr, \quad (22)$$

and from an analogous analysis the tunneling from the conduction band to the valence band (J_{VC}) is obtained.

Therefore, Sentaurus Device uses a different approach to evaluate the transversal momentum of the carriers that are involved in a tunneling process. It is not explicit in the expression of the tunneling current but it is accounted for through the double integral over the energy and space. Moreover, the Sentaurus Device uses the carrier temperatures instead of the lattice temperature to calculate the tunneling recombination. Our simulator and Atlas assume that both temperatures are the same.

4. Tunneling current results

First of all, we simulated the I–V characteristic of a GaAs and a ZnO tunnel junctions using Atlas [24] from Silvaco and Sentaurus Device [25] from Synopsys, two standard commercial tools. The results were compared with those from our simulator in order to check its performance. The calculations were done using the parameters listed in table 1 for GaAs and in table 2 for ZnO which describe well most experimental observations and are consistent with the data presented in literature [3, 29–31].

Figure 4 shows results for the tunneling current in a GaAs diode with constant doping levels of $N_A = 2 \times 10^{20}$ cm^{-3} in the p–side and $N_D = 3 \times 10^{18}$ cm^{-3} in the n–side and a ZnO diode with $N_A = 1 \times 10^{20}$ cm^{-3} and $N_D = 1 \times 10^{20}$ cm^{-3}. These values are in the range of the typical concentration levels in a ferromagnetic diode. The values are also chosen to have the same relation between the distances of the Fermi level to the band edged

Table 1: Suitable parameters for GaAs.

GaAs parameters	
Parameter	Value
Band gap energy (E_g)	1.4 eV
Electron affinity (χ)	4.2 eV
Dielectric constant (static ϵ)	$13.2\epsilon_0$
Dielectric constant (optical ϵ)	$3.5\epsilon_0$
Electron effective mass (m_e^*)	$0.067m_0$
Hole effective mass (m_h^*)	$0.47m_0$
Effective density of states in conduction band (N_c)	4.4×10^{17} cm^{-3}
Effective density of states in valence band (N_v)	8.5×10^{18} cm^{-3}
Electron mobility	8500 cm^{2}V^{-1}s^{-1}
Hole mobility (μ_p)	400 cm^{2}V^{-1}s^{-1}

Table 2: Suitable parameters for ZnO. $E||c$ meas parallel polarization and $E\perp c$ perpendicular polarization of the electric field to the optical axis.

ZnO parameters	
Parameter	Value
Band gap energy (E_g)	3.3 eV
Electron affinity (χ)	4.1 eV
Dielectric constant (static ϵ)	$E\perp c$ $7.6\epsilon_0$
	$E\|\|c$ $8.5\epsilon_0$
Dielectric constant (optical ϵ)	$E\perp c$ $3.6\epsilon_0$
	$E\|\|c$ $3.7\epsilon_0$
Electron effective mass (m_e^*)	$0.27m_0$
Hole effective mass (m_h^*)	$0.54m_0$
Effective density of states in conduction band (N_c)	3.5×10^{18} cm^{-3}
Effective density of states in valence band (N_v)	1×10^{19} cm^{-3}
Electron mobility (μ_n)	$100 - 300$ cm^{2}V^{-1}s^{-1}
Hole mobility (μ_p)	$0.1 - 6$ cm^{2}V^{-1}s^{-1}

but having a majority of holes in the GaAs diode and a majority of electrons in the ZnO as it occurs naturally in ferromagnetic GaAs and ZnO, which are naturally p–type and n–type, respectively, when they are doped with magnetic impurities.

The results from the simulations run at different temperatures show the same result for the band diagram from our simulator and the commercial versions, figures 4a and 4b. However, the tunneling current presents different behaviors depending on the tool. The results at 300 K, figure 4c for GaAs and figure 4d for ZnO, show quite similar behavior between our simulator and Atlas, as we expected because we use an equivalent model for the tunneling current. Sentaurus results are different because it uses a different approximation to treat the transversal energies and can lead to the larger tunneling current near to the valley voltages. However, at low temperatures the tunneling current has different behavior for all the three simulators, figure 4e for GaAs and figure 4f for ZnO. The strange be-

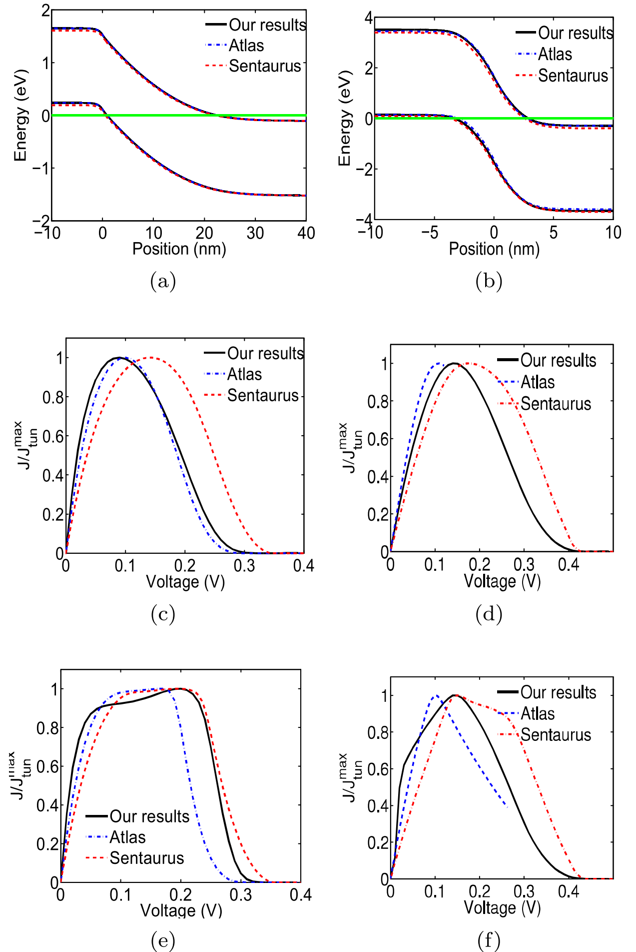

Figure 4: Simulation of tunnel diodes based on GaAs with constant doping levels of $N_A = 2 \times 10^{20}$ cm^{-3} and $N_D = 3 \times 10^{18}$ cm^{-3} and ZnO with $N_A = 1 \times 10^{20}$ cm^{-3} and $N_D = 1 \times 10^{20}$ cm^{-3}. The figures show the band diagram for GaAs (a) and for ZnO (b), the tunneling current for GaAs (c) and ZnO (d) at room temperature; and the tunneling current for GaAs (e) and ZnO (f) at 77 K. The calculations where performed using three different tools: our in–house simulator, Atlas from Silvaco and Sentaurus from Synopsys.

havior of our simulator at very low voltages comes from instabilities in the pseudo–Fermi levels calculations due to the small current values, but they tend to disappear rapidly as the bias rises. However, they do not explain the differences at around and over the peak voltage. This can be due to the different approximations for the Fermi–Dirac carrier distribution, more important at low temperatures.

We note that the value of the smaller relative Fermi energy ε_S, ε_n for GaAs and ε_p for ZnO, determines the maximum tunneling current for a bias ε_S/q_e. Since it is desirable to look for polarization dependence of the tunneling current near the voltage where the total tunneling current is a maximum it is clear that any change in the smaller of the two Fermi energies will drive the TMR behavior in the junction.

With these results, we want to show that the different implementations of the non–local tunneling current model

lead to very different results making it impossible to calibrate our simulator using commercial tools. Another important reason to not be worried about these differences is that when the band splits due to the ferromagnetism, the tunneling current becomes very dependent on the model that is used to simulate the spin polarization in the depletion region of the junction. Therefore, the results from our simulator are considered valid because, despite the differences among the three tools, they all show the same behavior for the results of the tunneling current and the obtained values of the peak and valley biases are in agreement with prediction of the Kane's model for the tunneling current [27].

5. Spin split bands

The effect of the exchange interaction between the charge carriers and the localized magnetic moments on the energy band structure and the transport properties can be estimated by using a perturbation theory [32]. A first order correction of the band energies due to the exchange potential can be written as:

$$E_{\mathbf{k}\sigma} = E^0_{be} + \frac{\hbar^2\mathbf{k}^2}{2m^*} - \frac{\Delta}{2}\left(\delta_{\sigma\uparrow} - \delta_{\sigma\downarrow}\right), \tag{23}$$

where $\Delta = xJ_{exch}\langle S^z\rangle$ is the fist–order band splitting. In the mean field approximation, the average spin polarization of the magnetic moments, $\langle S^z\rangle$, is given by $x\langle S^z\rangle = xSB_S(y)$, where x is the concentration of Mn ions and $B_S(y)$ is the Brioullin function for the spin S.

Figure 5 shows the calculated band splitting of the band edge for (GaMn)As using this first order approach of the exchange interaction with $J^{pd}_{exch} = 1.4\ eV$, $m^* = 0.5m_0$, $T_C = 110\ K$ and $S = 5/2$. The band splitting disappears for temperatures over T_C at $B = 0$ and rises to a maximum value for low temperatures.

When the bands edges are spin–split, there are two different characteristic energies [4, 33] for the occupations for each spin $\varepsilon^\sigma_n = E_{Fn} - E^\sigma_C = E_{Fp} - E_C \pm \Delta_n/2$ and $\varepsilon^\sigma_p = E^\sigma_V - E_{Fp} = E_V \pm \Delta_p/2 - E_{Fp}$, with $\sigma = (\uparrow, \downarrow)$. The tunneling occurs between the two majority and the two minority bands or, if the relative magnetization of the layer is reversed, between the majority and the minority bands, see figure 6. We call these currents antiparallel current $I_{ap}(V)$, figure 6a, and parallel current $I_p(V)$, figure 6b, respectively. The tunneling recombination term is reevaluated for each spin–band obtaining four recombination terms related with the $e^\uparrow$–$h^\downarrow$ and the $e^\downarrow$–$h^\uparrow$ recombinations. The maximum value of $\Delta_{n,p}$ occurs when the band is fully polarized. The Fermi energies are adjusted so that the total number of carriers stays constant as Δ changes. The spin polarization for each band defined as:

$$P = \frac{|n^\uparrow - n^\downarrow|}{(n^\uparrow + n^\downarrow)}; \tag{24}$$

clearly $P = 1$ when the band is fully spin–polarized and $P = 0$ when the band is unpolarized.

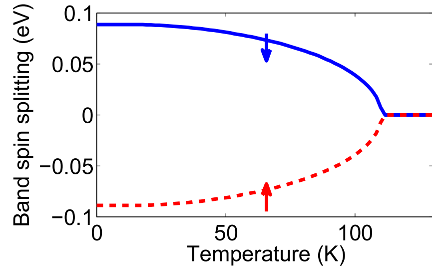

Figure 5: Temperature dependence of the band edge in (GaMn)As, $T_C = 110\ K$.

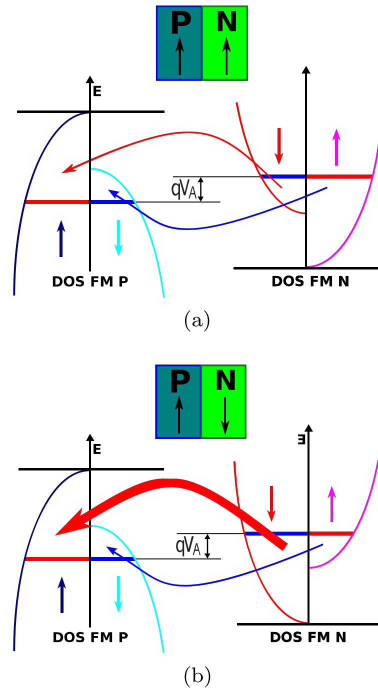

Figure 6: Schematic of the spin–split bands for the antiparallel (a) and parallel (b) configuration. The arrows show the tunnel recombination processes.

To calculate the spin splitting we suppose that the total carrier concentration remains constant when the spin is polarized, $n^0 = n^\uparrow + n^\downarrow$ and $p^0 = p^\uparrow + p^\downarrow$, where n^0 and p^0 are the electron and hole concentrations with no spin polarization. In this work we have made the assumption that the spin polarization ratio is conserved in each device region. To study the ferromagnetic and the antiferromagnetic interactions between the p and n sides, which correspond to the antiparallel and parallel configurations, we considered that the spin flip occurs in the depletion region, in the point where the carrier concentration reaches its minimum, because in that point the carrier mediated exchange interaction has to be weaker.

If a Zener diode with both sides ferromagnetic is taken around a hysteresis loop it should show a butterfly loop with TMR defined as the relative difference between the currents in parallel and antiparallel configurations,

$$\mathrm{TMR}(V) = \frac{|I_p(V) - I_{ap}(V)|}{I_p(V) + I_{ap}(V)} \times 100\%, \tag{25}$$

as a function of field because the magnetizations of the two components would be parallel at large fields but would be antiparallel at some intermediate field value [34]. In the unlikely event of both sides being 100% polarized the minority spin concentration will be zero and $I_{ap}(V)$ would vanish leading to TMR= 100% at all voltages in the tunneling regime.

6. Results for GaAs

The tunneling current in the ferromagnetic case was calculated for a range of parameters appropriate to GaAs, see table 1. We show the results in two cases, when $\varepsilon_n = \varepsilon_p$, i.e., when both sides have same degeneration levels, and when $\varepsilon_n < \varepsilon_p$, the more realistic configuration for Co or Mn doped GaAs. We consider a temperature of 77 K, a standard lab temperature well below the largest known Curie temperature for ferromagnetic GaAs ($T_C \sim 164$ K). Figure 7a shows the obtained band diagram for a diode with the same degeneration level in each side. We have chosen $\varepsilon_{n,p} = 0.2eV$ as the carrier concentrations are in the range of experimental devices. Note that the depletion region on the p side in much smaller as the density of states in the valence band is one order of magnitude higher than in the conduction band, and therefore larger doping is necessary to achieve the same degeneration level. Figure 7a also shows the spin–split bands obtained considering a carrier spin–polarization of 90%. The band for each spin can be identified using the color schema shown in figure 6. Figure 7b shows that the TMR has small values when the bias is less than $\varepsilon_S/q_e = min(\varepsilon_n, \varepsilon_p)/q_e \sim 0.2$ V and it quickly increases its value in the NRR, then the effect of the spin polarization is easier to see in the NRR.

Figure 8 shows the parallel and antiparallel current densities, calculated at different spin–polarization ratios at 77 K for a diode with same degeneration levels in both

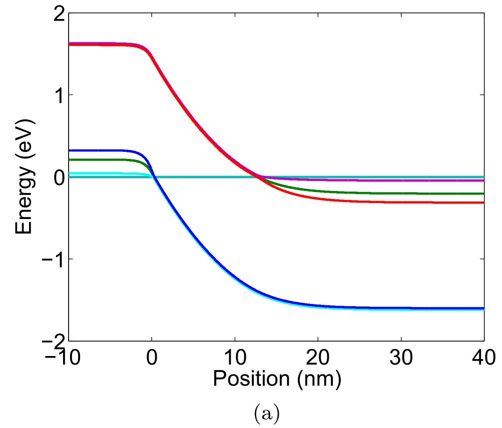

(a)

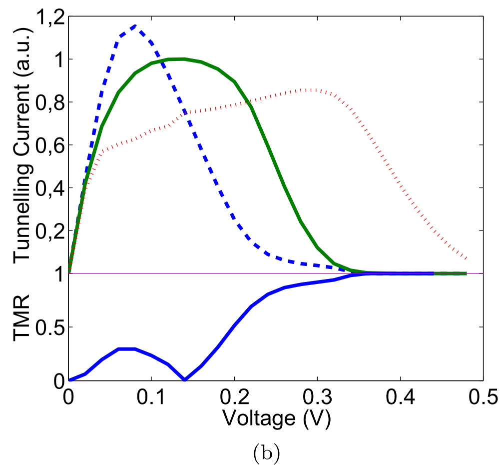

(b)

Figure 7: (a) Band structure for a ferromagnetic GaAs diode with the same degeneration level in each side, $\varepsilon_{n,p} = 0.2$ eV, which corresponds with hole concentration of 1.5×10^{20} cm^{-3} in the p neutral region and a electron concentration of 7.3×10^{18} cm^{-3} in the n neutral region and (b) the tunnel current density for a non–ferromagnetic diode (continuous green line), for the parallel configuration (dashed blue line) and for antiparallel configuration (dot–dashed red line); the TMR (continous blue line) is also presented. Both results are obtained assuming a constant spin–polarization ratio of 90%.

sides. The bias was chosen to be halfway down the NRR, $V = 0.25$ V, to have a trade–off between the rising TMR at larger biases that we obtain from our simulations, and the possible degradation of the TMR due to trap assisted tunneling and diffusion current that we do not account for in our simulations. As expected, the TMR shows higher values as the carrier polarization increases and also, at this bias, has good agreement with the predicted values from Jullière formula [34]:

$$TMR = \frac{2 \times P_{left} \times P_{right}}{1 + P_{left} \times P_{right}}, \tag{26}$$

where P_{left} and P_{right} are the polarization levels in the left and right side of the junction respectively, namely the p side and the n side.

Even though we expected some agreement with Jullière's prediction, these coincidences are surprising because Jullière's

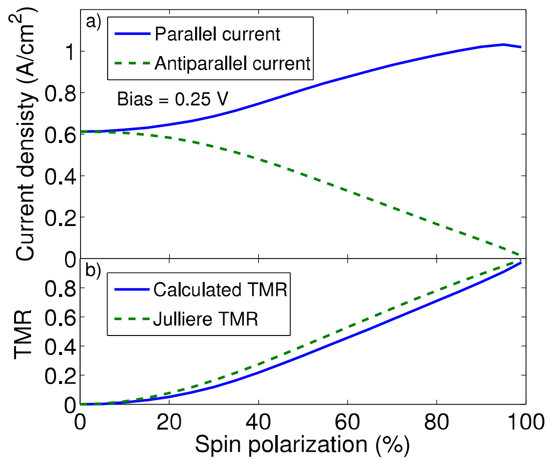

Figure 8: Parallel and the antiparallel current densities and TMR, calculated at different spin–polarization ratios at 77 K for a GaAs diode with same degeneration levels in both sides

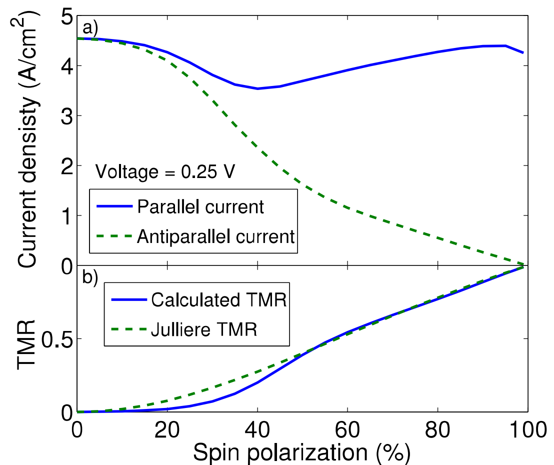

Figure 9: Parallel and the antiparallel current densities and TMR, calculated at different spin–polarization ratios at 77 K for a GaAs diode degeneration levels of $\varepsilon_p = 0.3$ eV and $\varepsilon_n = 0.1$ eV

theory was formulated for thin film tunnel structures composed of two ferromagnetic metallic electrodes (Fe, Co, Pb) with a semiconductor layer (Ge) in the middle which acts as tunnel barrier. Moreover, the measurements that supported this theory were made at very low temperatures (4.7 K). Therefore, it would be reasonable to see a better match between our results and Jullière's at lower temperatures, but we found the opposite. Further work in this direction will be performed to gain better understanding of these phenomena. However, we want to recall that our structure is a bipolar tunnel junction (both the valence and conduction bands participate in the conduction), while Julliere's structure is a unipolar device (only the conduction band is relevant), and the tunneling barrier properties are very dependent on the bias and spin–polarization degree.

The calculations were repeated for a more realistic configuration, this is, considering different degeneration levels in each side of the junction. In this case we consider carrier concentrations observed in experiments, a hole concentration of 2.5×10^{20} cm^{-3} in the p neutral region and a electron concentration of 3×10^{18} cm^{-3} in the n neutral region, which means degenerations levels of $\varepsilon_L = \varepsilon_p = 0.3$ eV and $\varepsilon_S = \varepsilon_n = 0.1$ eV. The selected bias to extract the TMR is again $V = 0.25$ as the maximum of the tunneling current is around 0.1 V and it disappears at 0.4 V. The results are shown in figure 9.

7. Results for ZnO

The same procedure was followed to simulate the diode based on ZnO, using the parameters listed in table 2. We show the results in two cases, when $\varepsilon_n = \varepsilon_p$, this is when both sides have same degeneration levels, and when $\varepsilon_p < \varepsilon_n$, the more realistic configuration for Co or Mn doped ZnO as it is naturally a n type semiconductor. Now we consider a temperature of 77 K to make possible a comparison between GaAs and ZnO results, but we have also made simulation at 300 K as the Curie temperature for ZnO is expected to be larger than room temperature. Figure 10a shows the obtained band diagram for a diode with the same degeneration level in each side, we have chosen again $\varepsilon_{n,p} = 0.2$ eV.

Now the depletion regions are more similar as the density of states in valence and conduction bands are closer to each other. Again, figure 10a also shows the spin–split bands obtained considering a carrier spin–polarization of 90%, the band for each spin can be identified using the color schema show in figure 6. The wider band–gap of the ZnO leads to a much narrower depletion region, and therefore the equivalent tunneling barrier is also narrower, i.e., larger values of the tunneling current. However, the tunneling current is proportional to the square root of the tunneling masses of the involved carriers (see equation 17), which are difficult to determine, hence the tunneling current need to be calibrated from experimental measurements. Therefore, our results are normalized to the maximum tunneling current value in the non–ferromagnetic case because the TMR value does not depend on the absolute value but in the relative difference between the parallel and the antiparallel configurations.

The parallel and the antiparallel current densities and the TMR for a ZnO diode with same degeneration levels in both sides are shown in figure 11a at a temperature of 77 K and figure 11b at 300 K. Now the halfway bias down the NRR is chosen to be $V = 0.3$ V as the peak tunneling current occurs at a bias closer to 0.2 V. Again the TMR shows higher values as the carrier polarization increases and also has good agreement with the predicted values by Jullière's formula, especially at 300 K where the result from simulation is equal to the predicted values. At 77 K the Jullière's formula overestimates the TMR having a larger difference than in the GaAs case.

The calculations were repeated for the more realistic configuration, i.e., considering different degeneration lev-

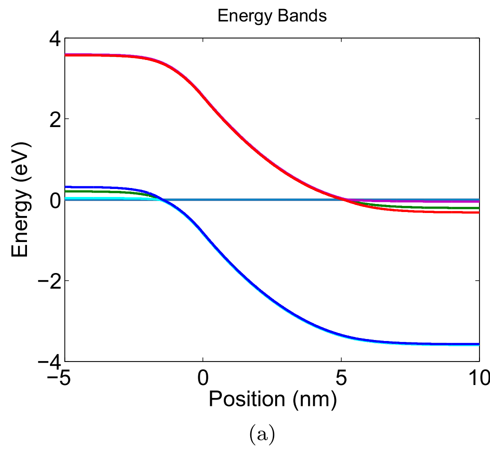

(a)

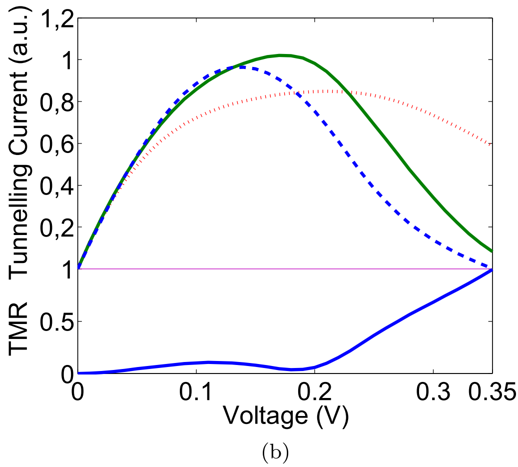

(b)

Figure 10: (a) Band structure for a ferromagnetic ZnO diode with the same degeneration level in each side, $\varepsilon_{n,p} = 0.2$ eV, which corresponds with hole concentration of 1.7×10^{20} cm^{-3} in the p neutral region and a electron concentration of 6×10^{19} cm^{-3} in the n neutral region and (b) the tunnel current density for a non–ferromagnetic diode (continuous green line), for the parallel configuration (dashed blue line) and for antiparallel configuration (dot–dashed red line); the TMR (continuous blue line) is also presented. Both results are obtained assuming a constant spin–polarization ratio of 90%

els in each side of the junction. In this case we consider carrier concentrations observed in experiments, a hole concentration of 3.1×10^{18} cm^{-3} in the p neutral region and an electron concentration of 1.3×10^{19} cm^{-3} in the n neutral region, to observe the n character of the ZnO. These carrier concentrations result in degenerations levels of $\varepsilon_S = \varepsilon_p = 0.017$ eV and $\varepsilon_L = \varepsilon_n = 0.02$ eV. The selected bias to extract the TMR is again 0.12 V as the maximum of the tunneling current is around 0.05 V and it disappears at 0.2 V. The results are shown in figure 12a for simulations done at 77 K and in 12b for 300 K.

Once more, the results at 300 K show better agreement with the TMR predicted using the Jullière's formula in both cases presented for ZnO. Moreover, in the last case at low temperature (figure 12a) the antiparallel current shows a different behavior from previous configurations. It starts rising as the spin polarization ratio goes up until

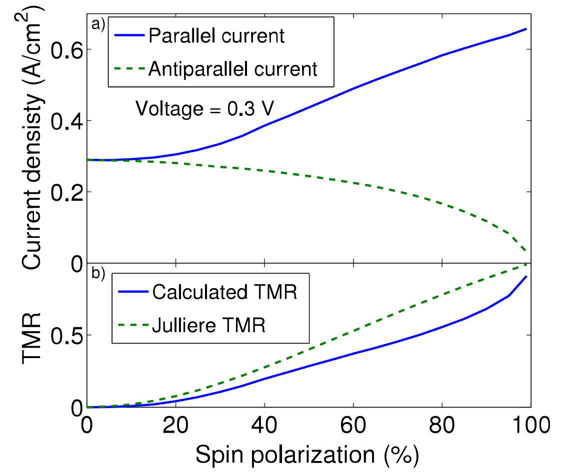

(a)

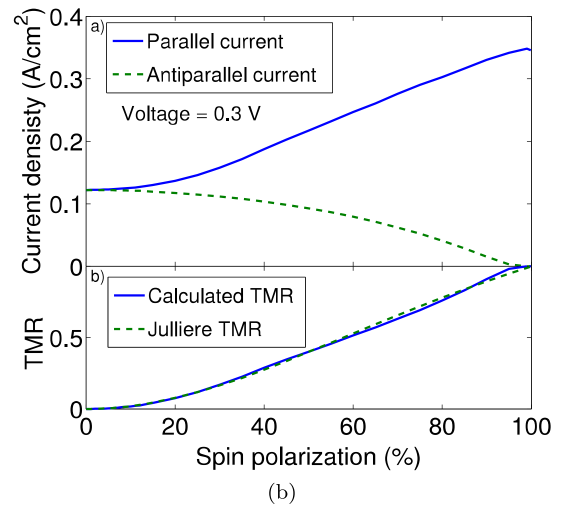

(b)

Figure 11: Parallel and the antiparallel current densities and TMR, calculated at different spin–polarization ratios for a ZnO ferromagnetic diode with same degeneration levels in both sides at (a) 77 K and (b) 300 K.

a 90% ratio is reached and then decreases rapidly. We found that this anomaly is produced by the combination of two factors:

1. The low level of degeneration in the p–side which leads to a much lower hole concentration than the electron concentration in the n–side. Because of this the band splitting in the n–side, at a certain spin–polarization value, is smaller than in the p–side due to lower magnetization values (see figure 13). Therefore, the difference between the parallel and antiparallel configuration is mostly dominated by the side with larger carrier concentration, in this case the n–side.
2. The energy carrier distributions in the valence and conduction bands are described by the Fermi–Dirac function. Therefore, at lower temperatures the kinetic energy of the carriers drops and they occupy energy levels close to the band edges, thus making them available to tunneling and increasing the over-

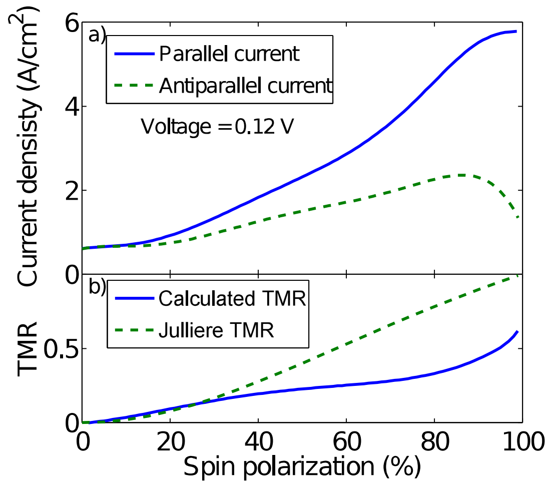

(a)

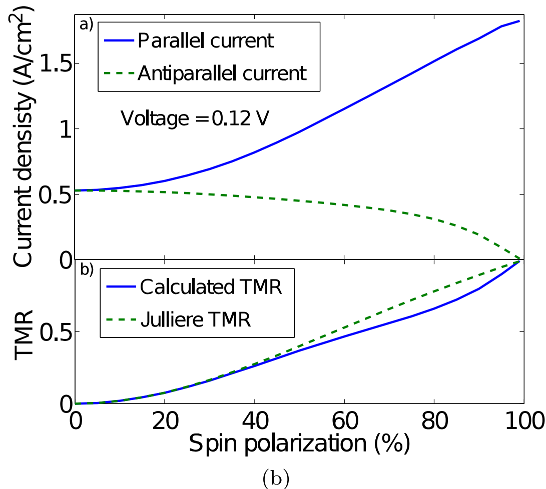

(b)

Figure 12: Parallel and the antiparallel current densities and TMR, calculated at different spin–polarization ratios for a ZnO ferromagnetic diode degeneration levels of $\varepsilon_p = 0.3$ eV and $\varepsilon_n = 0.1$ eV at (a) 77 K and (b) 300 K.

lapping value between the two valence and conduction bands, as described in equation (18).

As the temperature drops, carrier tunneling will be favored in two ways: 1) the increase of the carrier concentration in the allowed energy range for tunneling and 2) the decrease of the tunneling barrier height due to band splitting. Both will be higher as the spin–polarization is increased.

8. Conclusions

In this paper we show the results from the simulations performed for GaAs and ZnO ferromagnetic diodes. Firstly we show how different available simulators offer very different results for the tunneling current even when they implement the same non–local model for the direct tunneling current, but using different approaches. We show the results obtained for the tunneling current from

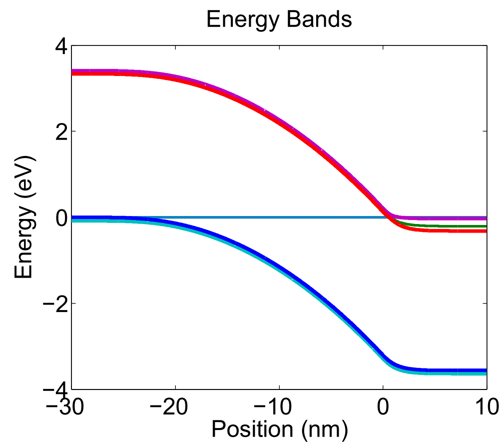

Figure 13: Band structure for a ferromagnetic ZnO diode with the different degeneration level in each side, $\varepsilon_S = \varepsilon_p = 0.017$ eV and $\varepsilon_L = \varepsilon_n = 0.02$ eV, which corresponds with a hole concentration of 3.1×10^{18} cm^{-3} in the p neutral region and an electron concentration of 1.3×10^{19} cm^{-3} in the n neutral region.

the commercial tools Atlas from Silvaco and Sentaurus Device from Synopsys and they are compared with the results obtained from our in–house simulator. Secondly, we have added the effect of the ferromagnetism on the carrier spin–polarization that our simulator accounts for using a spin–splitting of the band edges driving to two different energy bands depending on which carrier spin we consider. We have compared the results obtained for the tunneling current in ferromagnetic GaAs and ZnO diodes under different magnetization levels and at different relevant temperatures using the TMR signal.

We compared our results with Jullière's formula and we found good agreement at room temperature even though it was formulated for low temperature. Further work will be performed to gain better understanding of these phenomena in our device. However, due to the large number of variables participating on the value of the TMR (valence band and conduction band polarization, temperature, biases and electron and hole concentrations), we consider the numerical simulation that we propose here a more general way to predict the TMR in this kind of structures. Additionally, it offers a trade–off between the more simplistic analytical methods, such as Jullière's formula, and those based on ab–initio calculations, like density functional calculations and non–equilibrium Green's functions [35], which are much more computationally expensive.

From the results shown before for GaAs and ZnO ferromagnetic diodes, it seems that the wider band–gap of the ZnO diode leads to lower TMR under the same conditions even when the tunneling current is more intense in the ZnO. However the TMR behavior at room temperature for ZnO shows a better agreement with the TMR values predicted using the Jullière's formula for both cases, same degeneration level and different degeneration level in the n and p sides. We have shown that larger band–gap mate-

rials could show lower TMRs; however, the possibility to operate at room temperatures wide band–gap DMSs may provide larger values of the TMR.

Acknowledgments

Work supported by Spanish Government under the project MCYT TIN2007-67537-C03-01, the Ministry of Education and Science of Spain, Xunta de Galicia and FEDER funds under project TEC2010-17320 and contracts 2010/28 and 09TIC001CT.

References

References

[1] H. Akinaga, H. Ohno, Semiconductor Spintronics, IEEE Transactions On Nanotechnology 1 (1) (2002) 19–31. doi:10.1109/TNANO.2002.1005423.
URL http://ieeexplore.ieee.org/lpdocs/epic03/wrapper.htm?arnumber=1005423

[2] T. Dietl, H. Ohno, F. Matsukura, J. Cibert, D. Ferrand, Zener model description of ferromagnetism in zinc–blende magnetic semiconductors, Science 287 (5455) (2000) 1019–1022.
URL http://www.sciencemag.org/cgi/content/abstract/287/5455/1019

[3] T. Jungwirth, J. Sinova, J. Mašek, J. Kučera, A. H. MacDonald, Theory of ferromagnetic (III,Mn)V semiconductors, Reviews of Modern Physics 78 (3) (2006) 809.
URL http://link.aps.org/abstract/RMP/v78/p809

[4] H. Holmberg, N. Lebedeva, S. Novikov, P. Kuivalainen, M. Malfait, V. V. Moshchalkov, Electrical transport in Mn-doped GaAs pn-diodes, Physica Status Solidi (a) 204 (2007) 791–804.
URL http://dx.doi.org/10.1002/pssa.200622448

[5] Z. Deng, C. Q. Jin, Q. Q. Liu, X. C. Wang, J. L. Zhu, S. M. Feng, L. C. Chen, R. C. Yu, C. Arguello, T. Goko, F. Ning, J. Zhang, Y. Wang, A. A. Aczel, T. Munsie, T. J. Williams, G. M. Luke, T. Kakeshita, S. Uchida, W. Higemoto, T. U. Ito, B. Gu, S. Maekawa, G. D. Morris, Y. J. Uemura, Li(Zn,Mn)As as a new generation ferromagnet based on a I-II-V semiconductor, Nature Communications 2 (2011) 422. doi:10.1038/ncomms1425.
URL http://www.nature.com/ncomms/journal/v2/n8/full/ncomms1425.html

[6] P. N. Hai, L. D. Anh, S. Mohan, T. Tamegai, M. Kodzuka, T. Ohkubo, K. Hono, and M. Tanaka, Growth and characterization of n-type electron-induced ferromagnetic semiconductor (In,Fe)As, arXiv:1209.0250 [cond-mat.mtrl-sci] (2012).
URL http://arxiv.org/abs/1209.0250

[7] A. Ney, V. Ney, S. Ye, K. Ollefs, T. Kammermeier, T. Kaspar, S. Chambers, F. Wilhelm, A. Rogalev, Magnetism of Co doped ZnO with Al codoping: Carrier-induced mechanisms versus extrinsic origins, Physical Review B 82 (4). doi:10.1103/PhysRevB.82.041202.
URL http://link.aps.org/doi/10.1103/PhysRevB.82.041202

[8] A. Serrano, E. Pinel, A. Quesada, I. Lorite, M. Plaza, L. Pérez, F. Jiménez-Villacorta, J. de La Venta, M. Martín-González, J. Costa-Krämer, J. Fernandez, J. Llopis, M. García, Room-temperature ferromagnetism in the mixtures of the TiO2 and Co3O4 powders, Physical Review B 79 (2009) 144405. doi:10.1103/PhysRevB.79.144405.
URL http://link.aps.org/doi/10.1103/PhysRevB.79.144405

[9] A. Espinosa, M. García-Hernández, N. Menéndez, C. Prieto, A. de Andrés, Ferromagnetism in SnO_2–based multilayers: Clustering of defects induced by doping, Physical Review B 81 (2010) 064419. doi:10.1103/PhysRevB.81.064419.
URL http://link.aps.org/doi/10.1103/PhysRevB.81.064419

[10] M. Ding, D. Zhao, B. Yao, B. Li, Z. Zhang, and D. Shen, The p-type ZnO film realized by a hydrothermal treatment method, Applied Physics Letters 98 (6) (2011) 062102. doi:10.1063/1.3549304.
URL http://link.aip.org/link/APPLAB/v98/i6/p062102/s1&Agg=doi

[11] Y. J. Huang, M. F. Shih, C. P. Chou, K. Y. Lo, and S. Y. Chu, Fabrication of p-Type ZnO Films Grown on Arsenic-Implanted Silicon via Thermal Diffusion at Various Substrate Temperatures, ECS Journal of Solid State Science and Technology 1 (5) (2012) 276. doi:10.1149/2.018206jss.
URL http://jss.ecsdl.org/cgi/doi/10.1149/2.018206jss

[12] C. Song, X. J. Liu, F. Zeng, F. Pan, Fully epitaxial (Zn,Co)O/ZnO/(Zn,Co)O junction and its tunnel magnetoresistance, Applied Physics Letters 91 (4) (2007) 042106. doi:10.1063/1.2762297.
URL http://link.aip.org/link/APPLAB/v91/i4/p042106/s1\&Agg=doi

[13] G. Chen, F. Zeng, F. Pan, Enhanced spin injection and voltage bias in (Zn,Co)O/MgO/(Zn,Co)O magnetic tunnel junctions, Applied Physics Letters 95 (23) (2009) 232508. doi:10.1063/1.3271776.
URL http://link.aip.org/link/APPLAB/v95/i23/p232508/s1\&Agg=doi

[14] T. Fukumura, H. Toyosaki, Y. Yamada, Magnetic oxide semiconductors, Semiconductor Science and Technology 20 (4) (2005) S103–S111. doi:10.1088/0268-1242/20/4/012.
URL http://stacks.iop.org/0268-1242/20/i=4/a=012?key=crossref.155ca983403f0206fec0dc910268994d

[15] D. C. Kundaliya, S. B. Ogale, S. E. Lofland, S. Dhar, C. J. Metting, S. R. Shinde, Z. Ma, B. Varughese, K. V. Ramanujachary, L. Salamanca-Riba, T. Venkatesan, On the origin of high-temperature ferromagnetism in the low-temperature-processed Mn-Zn-O system., Nature materials 3 (10) (2004) 709–14. doi:10.1038/nmat1221.
URL http://www.ncbi.nlm.nih.gov/pubmed/15448682

[16] X. H. Xu, H. J. Blythe, M. Ziese, A. J. Behan, J. R. Neal, A. Mokhtari, R. M. Ibrahim, A. M. Fox, G. A. Gehring, Carrier-induced ferromagnetism in n-type ZnMnAlO and ZnCoAlO thin films at room temperature, New Journal of Physics 8 (8) (2006) 135.
URL http://stacks.iop.org/1367-2630/8/135

[17] S. M. Sze, K. K. Ng, Physics of Semiconductor Devices, 3rd Edition, John Wiley & Sons, Inc., New Jersey, US, 2006.

[18] P. Sankowski, P. Kacman, J. Majewski, T. Dietl, Spin-dependent tunneling in modulated structures of (Ga,Mn)As, Physical Review B 75 (4). doi:10.1103/PhysRevB.75.045306.
URL http://link.aps.org/doi/10.1103/PhysRevB.75.045306

[19] G. van der Laan, K. Edmonds, E. Arenholz, N. Farley, B. Gallagher, Valence-state model of strain-dependent Mn L(2,3) x-ray magnetic circular dichroism from ferromagnetic semiconductors, Physical Review B 81 (21) (2010) 214422. doi:10.1103/PhysRevB.81.214422.
URL http://link.aps.org/doi/10.1103/PhysRevB.81.214422

[20] E. Comesaña, G. A. Gehring, Spin polarised tunnelling in a ferromagnetic Zener diode, Applied Physics Letters 91 (2007) 142510.
URL http://link.aip.org/link/?APPLAB/91/142510/1

[21] E. Comesaña, M. Aldegunde, G. A. Gehring, A. J. Garcia-Loureiro, Numerical simulation of a ferromagnetic spin-polarised diode, in: 2009 Spanish Conference on Electron Devices, IEEE, 2009, pp. 160–163. doi:10.1109/SCED.2009.4800455.
URL http://ieeexplore.ieee.org/lpdocs/epic03/wrapper.htm?arnumber=4800455

[22] I. Zutic, J. Fabian, S. C. Erwin, Bipolar spintronics: Fundamentals and applications, IBM Journal of Research and Development 50 (1) (2006) 121–139. doi:10.1147/rd.501.0121.
URL http://ieeexplore.ieee.org/lpdocs/epic03/wrapper.htm?arnumber=5388782

[23] M. I. Miah, E. M. Gray, Spin drift–diffusion transport

and its applications in semiconductors, Current opinion in solid state and materials science 13 (5-6) (2009) 99–104. doi:10.1016/j.cossms.2009.02.002.
URL http://linkinghub.elsevier.com/retrieve/pii/S1359028609000096

[24] ATLAS User's Manual, Silvaco, Inc., Santa Clara, 2010.

[25] Sentaurus Device user guide, d-2010.03 Edition, Synopsys, Inc., Mountain View, 2010.

[26] D. Schroeder, T. Ostermann, O. Kalz, Comparison of transport models far the simulation of degenerate semiconductors, Semiconductor Science and Technology 9 (4) (1994) 364–369. doi:10.1088/0268-1242/9/4/005.
URL http://stacks.iop.org/0268-1242/9/i=4/a=005?key=crossref.9481236ff5e3b56ff2cb67851d33a54f

[27] E. O. Kane, Theory of tunneling, Journal of Applied Physics 32 (1) (1961) 83–91.
URL http://link.aip.org/link/?JAP/32/83/1

[28] G. Wachutka, An Extended Thermodynamic Model for the Simultaneous Simulation of the Thermal and Electrical Behaviour of Semiconductor Devices, in Proceedings of the Sixth International Conference on the Numerical Analysis of Semiconductor Devices and Integrated Circuits (NASECODE VI), Dublin, Ireland, (1989) 409.

[29] I. Vurgaftman, J. R. Meyer, L. R. Ram-Mohan, Band parameters for III–V compound semiconductors and their alloys, Journal of Applied Physics 89 (11) (2001) 5815. doi:10.1063/1.1368156.
URL http://link.aip.org/link/JAPIAU/v89/i11/p5815/s1\&Agg=doi

[30] J. D. Albrecht, P. P. Ruden, S. Limpijumnong, W. R. L. Lambrecht, K. F. Brennan, High field electron transport properties of bulk ZnO, Journal of Applied Physics 86 (12) (1999) 6864. doi:10.1063/1.371764.
URL http://link.aip.org/link/JAPIAU/v86/i12/p6864/s1\&Agg=doi

[31] U. Özgür, Y. I. Alivov, C. Liu, A. Teke, M. A. Reshchikov, S. Dogan, V. Avrutin, S.-J. Cho, H. Morkoç, A comprehensive review of ZnO materials and devices, Journal of Applied Physics 98 (4) (2005) 041301. doi:10.1063/1.1992666.
URL http://link.aip.org/link/JAPIAU/v98/i4/p041301/s1\&Agg=doi

[32] N. Lebedeva, P. Kuivalainen, Modeling of ferromagnetic semiconductor devices for spintronics, Journal of Applied Physics 93 (12) (2003) 9845–9864.
URL http://link.aip.org/link/?JAP/93/9845/1

[33] G. A. Gehring, H. J. Blythe, A. J. Behan, A. M. Fox, R. M. Ibrahim, A. Mokhtari, J. R. Neal, Spintronic materials and technology, Vol. 14 of Series in Material Science and Engineering, Taylor & Francis, 2006, Ch. 1, pp. 3–37.

[34] M. Jullière, Tunneling between ferromagnetic films, Physics Letters A 54 (1975) 225–226.
URL http://www.sciencedirect.com/science/article/B6TVM-46R3N46-10D/2/90703cfc684b0679356dce9a76b2e942

[35] D. Waldron, L. Liu, and H. Guo, Ab initio simulation of magnetic tunnel junctions, Nanotechnology 18 (2007) 424026.
URL http://iopscience.iop.org/0957-4484/18/42/424026